Science of the Total Environment 692 (2019) 1135–1145

Contents lists available at ScienceDirect

Science of the Total Environment

journal homepage: www.elsevier.com/locate/scitotenv

The air pollution governed by subtropical high in a coastal city in Southeast China: Formation processes and influencing mechanisms

Xin Wu [a,b,c], Lingling Xu [a,b], Youwei Hong [a,b], Jinfang Chen [d], Yuqing Qiu [a,b,c], Baoye Hu [a,b,c], Zhenyu Hong [a,b,c], Yanru Zhang [a,b,c], Taotao Liu [a,b,c], Yantin Chen [a,b], Yahui Bian [a,b], Guoqing Zhao [a,b], Jinsheng Chen [a,b,*], Mengren Li [a,b,*]

[a] Center for Excellence in Regional Atmospheric Environment, Institute of Urban Environment, Chinese Academy of Sciences, Xiamen 361021, China
[b] Key Lab of Urban Environment and Health, Institute of Urban Environment, Chinese Academy of Sciences, Xiamen 361021, China
[c] University of Chinese Academy of Sciences, Beijing 100049, China
[d] College of Food and Biological Engineering, Jimei University, Xiamen 361021, China

HIGHLIGHTS

- Hourly $PM_{2.5}$ and O_3 showed similar trends during the WPSH transitory movement.
- A threshold at 28 °C of atmospheric oxidizing capacity was found.
- Aged sulfate and nitrate enhanced light extinction coupling with trajectories.

GRAPHICAL ABSTRACT

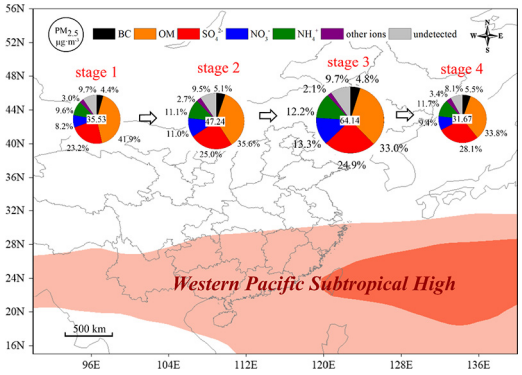

ARTICLE INFO

Article history:
Received 20 May 2019
Received in revised form 19 July 2019
Accepted 21 July 2019
Available online 22 July 2019

Editor: Jianmin Chen

Keywords:
Western Pacific subtropical high
Air pollution episode
Oxidation

ABSTRACT

To investigate the impact of the Western Pacific subtropical high (WPSH) on the air pollution episode of Xiamen, a coastal city in Southeastern China, this study focused on formation processes and influencing mechanisms of an air pollution episode from 17th to 23rd September 2017. The results showed that the WPSH fluctuated in this period and intensified this air pollution with local emissions. The episode was divided into four stages according to WPSH center locations to diagnose the air pollution. Visibility declined below 10 km twice while fine particulate matte ($PM_{2.5}$) concentration was up to 89.05 μg/m^3 during this episode. As a consequence of high temperature (28.33 ± 1.25 °C) resulted from WPSH, atmospheric oxidation at high level (140.81 ± 56.49 μg/m^3) was the driving force of secondary aerosols generations. Oxidation determined photo-chemical reactions with the pathways of gas-phase and heterogeneous formation. Sulfate was formed from gas-phase oxidation by SO_2 in daytime while heterogeneous reaction occurred at night. Nitrate generation was dominated by not only excess ammonium but also intense oxidation. Reconstruction light extinction results coupling with trajectories revealed that

* Corresponding authors at: Center for Excellence in Regional Atmospheric Environment, Institute of Urban Environment, Chinese Academy of Sciences, Xiamen 361021, China.
E-mail addresses: jschen@iue.ac.cn (J. Chen), mrli@iue.ac.cn (M. Li).

https://doi.org/10.1016/j.scitotenv.2019.07.341

Formation processes
Influencing mechanisms
Light extinction

$(NH_4)_2SO_4$, NH_4NO_3 and OM were the priority factors to the reduction of atmospheric visibility. These findings provided new insights of air pollution episode diagnosis and indicative function of WPSH impacts on local air quality in Southeast China.

1. Introduction

Atmospheric pollution is one of the most severe environmental problems of China in the past few decades. The effects of atmospheric pollution caused by fine particulate matters ($PM_{2.5}$) contained low visibility, unbalanced earth-atmosphere radiative budget, global climate changing and alerting human health (Watson, 2002; Ramanatha et al., 2001; Pope, 2000). The associated pollutants are emitted from anthropogenic and natural sources, then possibly secondary formed with chemical and photo-chemical reactions, but pollution is basically dominated by specific synoptic situations. Numerous studies have revealed the relationships between air pollution episodes and synoptic situations (Kalkstein and Corrigan, 1986; Greene et al., 1999; Zhang et al., 2015). Long regional transport of $PM_{2.5}$ by invoking the relatively stagnant air mass was the major source of severe air pollutions (Li et al., 2015). High concentrations of pollutants were found in stable air mass or under strong anticyclone control, whereas low concentrations occurred in moist, unstable air masses (Davis and Kalkstein, 1990).

Western Pacific subtropical high (WPSH) which influenced China directly is one of the warm high cells locating on Pacific (Tao and Chen, 1987; Ding, 1994). WPSH is evident as a semi-permanent, subtropical anticyclone high pressure system extending from the surface to the middle troposphere over the western North Pacific (Tao and Xu, 1962; Zhou et al., 2009). Zhao and Wang (2017) found that a stronger WPSH leads to a decrease of surface ozone over South China but an increase over North China and vice versa. He et al. (2012) found the abnormal behavior of the WPSH with a sudden northward movement had a direct impact on aerosol distribution characteristics.

Seasonal movement of WPSH cell between 10° and 40° north latitude leads to a series of variations of surface meteorology and atmospheric environment. Generally speaking, local air quality was better when the city was totally under control of WPSH. In fact, one small step move of WPSH might result in weather variations in one city, further caused air quality change. Hence, continuous shifts eastward and westward can possibly result in fluctuation of air quality. Atmospheric photo-oxidizing capability with high concentration of O_x depended on gaseous precursors and pre-existing aerosol, as well as high temperature and relative humidity which were common meteorological conditions accompanying with WPSH. Previous studies have proved oxidation processes and oxidizing capacity with different chemical signatures of regional air masses from different origins (Li et al., 2018). However, oxidation during WPSH such specific synoptic situation was lack of investigation. Furthermore, previous studies have illuminated the relationship between WPSH and air quality in long term, but the direct impact of WPSH on air pollution episode in short term still remained unknown. In this paper, a subtropical city in the southeast China, Xiamen (118.06°E, 24.61°N) was selected appropriately to study the role of WPSH in determining the air pollution episode. This city is influenced by WPSH >9 months every year and the transition to winter season was from September to November generally. In the transition to winter of 2017, a representative air pollution episode was captured from September 17th to 23rd. The objectives of this paper are to (1) explore the linkage between WPSH and this air pollution episode; (2) elucidate the impact of the atmospheric oxidation on influencing mechanisms of this air pollution episode; (3) probe into the contribution of chemical species of $PM_{2.5}$ to visibility reduction.

2. Material and methods

2.1. Synoptic data

The National Center for Environmental Prediction (NCEP) Final Operational Global Analysis data (FNL) are on 1-degree by 1-degree grids prepared operationally every 6 h. The FNLs are from the Global Data Assimilation System and made with the same model which NCEP uses in the Global Forecast System (GFS) (https://rda.ucar.edu/datasets/ds083.2/). The weather charts of surface layer, 850 hPa and 500 hPa were conducted in using Grid Analysis and Display System (GrADS) with the specific programmed script files.

2.2. Ground-based observation

The observation site is located on the rooftop of a twenty-floor building with 80 m high above ground level at Institute of Urban Environment, Chinese Academy of Sciences (118.06°E, 24.61°N). Thus, the local traffic emission is considered negligible. There is no major industrial source nearby and the nearest major industrial zone was about 10 km southwestward to the observation site.

Online hourly mass concentrations of particulate matters (PM_{10}, $PM_{2.5}$ and PM_1) were measured by using a tapered element oscillating microbalance (TEOM1405, Thermo Scientific Corp., MA, US). The tape was replaced when the load was >90% or over 1 month. Trace NO_2, SO_2 and O_3 gases were obtained with a resolution of 1 h by applying online analyzers (Thermo Instruments, TEI 42i, 43i and 49i, respectively). Air flow of the instruments was adjusted once a month. Before and after the monitoring periods, check was made with standard gases to ensure the reliability of each instrument performance. Ambient meteorological parameters including temperature (T), relative humidity (RH), wind speed (WS) and wind direction (WD) were obtained by an ultrasonic atmospherium (150WX, Airmar, the USA).

Vertical observation of light extinctions at 532 nm wavelengths and mixing layer process were retrieved from a high repetition rate lidar. Note that the mixing layer height was semi-quantified with extinction gradient method. Visibility was measured by a Belfort Model 6000 visibility sensor (Belfort Instrument Corp., MD, US). An integrated nephelometer at 3 wavelengths was used to obtain scattering coefficients (b_{scat}) (in using 525 nm wavelength) with internal relative humidity below 60%. The light chamber of nephelometer was cleaned in three months. Aethalometer at 7 wavelengths provided absorption coefficient (b_{abs}) (in using 520 nm wavelength) and black carbon (BC) concentration of ambient $PM_{2.5}$ (in using 880 nm wavelength). Aethalometer fiber tape was reloaded when the tape was <10%. In this paper, BC was equated with EC in discussion. Scattering and absorption coefficients were both averaged to one-hour resolution. $PM_{2.5}$ absorption coefficients were calculated based on the measured light attenuation (Zhuang et al., 2015).

$PM_{2.5}$ water-soluble inorganic ions (WSIIs) including SO_4^{2-}, NO_3^-, NH_4^+ and other ions were measured by Monitor for AeRosol and Gases in Ambient Air (MARGA) with one-hour resolution. For tracking changes in retention time and detector response for each sampling, the MARGA was continuously controlled by an internal calibration method using bromide for the anion chromatograph and lithium for the cation chromatograph over the whole observation period. The

internal calibration can ensure ion species to be identified and their corresponding concentrations to be measured successfully. Details on the MARGA are given elsewhere (Trebs et al., 2004). Organic matters (OM) were calculated from an aerosol chemical speciation monitor (ACSM) (Sun et al., 2015). All the real time monitoring measurements are summarized in Table S1.

2.3. Methodology

In this paper, three methods of extinction coefficients were employed to inquire the visibility variation. Retrieved extinction coefficient ($b_{ext,\ ret}$) was inversely correlated with visibility (V) according to the Koschmieder equation (Koschmieder, 1924) followed:

$$b_{ext,ret} = \frac{3.912}{V} \quad (1)$$

Measured extinction coefficient ($b_{ext,\ mea}$) and single scattering albedo (SSA) were calculated by b_{abs} and b_{scat} with the following equations:

$$b_{ext,mea} = b_{scat} + b_{abs} \quad (2)$$

$$SSA = \frac{b_{scat}}{b_{ext,mea}} \quad (3)$$

where b_{scat} and b_{abs} denoted scattering and absorption coefficients mentioned in Section 2.2. Wavelengths at about 520 nm (green light) could respond properly to the atmospheric visibility.

To investigate the contributions of $PM_{2.5}$ chemical components to light scattering and absorption, a revised formula developed by the original IMPROVE method is applied. Details of the revised IMPROVE formula can be found in Pitchford et al. (2007). Reconstructed extinction coefficients ($b_{ext,\ rec}$) in this paper also took NO_2 gas absorption into consideration, with the combination of directly measured b_{abs}.

To further refine the impact of WPSH position on the aerosol pollution in Xiamen, 24 h back trajectories from the sampling site were calculated using the NOAA HYSPLIT model. Different trajectories indicated different position of WPSH. The back trajectories were calculated each hour per day at starting times from 00:00 to 23:00 (LCT). Cluster analysis was then implemented to obtain trajectory clusters and average values of the light extinction coefficients with each cluster were calculated.

3. Results and discussion

3.1. Synoptic situation with air pollution

As a deep high pressure system, the WPSH is conventionally described by circulation patterns at 500 hPa with a characteristic isoline of 5880 gpm (geopotential meter) (Ding, 1994; Wang et al., 2006). This closed isoline encircles a large region over the western Pacific. A central isoline of 5920 gpm represented WPSH control center where there is stable circumstance and downdraft. WPSH shifted north or south along with seasonal alterations, while short term activities occurred from time to time. Usually, WPSH moves northward accompanied with westward shift and analogously southward with eastward movement. Short term activities occurred during transitions more often and could take a couple of days. Downdraft intensified gradually when the ridge stretched westward into inner land of East Asia, along with possible slight change of local air quality. Downdraft inside the WPSH brought sunny day and in fact, it also compressed mixing layer and/or aggravated air pollution consequently.

Fig. 1 demonstrated synoptic situations at 500hpa at the point time of each day from September 18th to 23rd. At the western sides of the WPSH, 500 hPa winds change directions from southeasterly to southwesterly during transition to winter. Pressure level at 500hpa was weak in 18th and WPSH center was blocked by Typhoon rear. WPSH ridge southward moved below 25 north latitude and fluctuated back and forth since the Sep 19. From 20th, WPSH started to strengthen gradually and shift northward. In 21st and 22nd, WPSH further westward shifted and basically dominated southeast China again. Mid-latitude westerlies were on the north side of the WPSH where the position of cold front was. Southerly flow in the west of the WPSH would bring adequate rainfall to dissipate air pollution. Lower surface pressure and warm high at the middle and lower layers in troposphere provided proper circulation background to pollution episode. On the surface layer (Fig. S1), the WPSH shifts more towards east and drives the low-level jet that transports a large amount of water vapor into East Asia (Lu, 2002). On the basis of WPSH position, the episode was divided to four stages subjectively: stage 1 was from the beginning to 2 am in 19th since the WPSH merged; stage 2 was from 3 am in 19th to 1 am in 21st when the WPSH began to eastward move slowly and fluctuated; stage 3 was from 2 am in 21st to 2 pm in 22nd when the WPSH moved westward; stage 4 was from 3 pm in 22nd to 0 am in 24th when the WPSH center controlled the southeastern coast.

Some of the significant parameters in four stages are listed in Table 1 and all of the data were averaged to represent the characteristics of four stages. Mixing layer process is a key factor in air quality to determine turbulence mixing, vertical diffusion, convective transport, cloud/aerosol entrainment and atmospheric pollutant deposition. Interactions between air pollution and mixing layer were identified in previous studies: low mixing layer structure and process suppressed air pollutants dispersion while air pollution promoted the formation of mixing layer (Sun et al., 2015; Petäjä et al., 2016). Mixing layer height (MLH) is one of the fundamental variables which influences many tropospheric processes critical to air pollution, such as aerosol distributions and haze formation (Seibert et al., 2000; Stevens, 2002; Lin et al., 2008; Konor et al., 2009). In Fig. 2, MLH was higher in stage 1 and 4 than that in stage 2 and 3. The MLH obviously declined in stage 1, then fluctuated in stage 2 and stayed below 1 km in stage 3, finally rose in stage 4.

Visibility is a good indicator for air quality and has been measured in numerous studies. The trend of visibility was similar to MLH in four stages which could confirm response of MLH to this air pollution episode. Visibility decreased to 10 km around in stage 3 while mixing layer height descended below 1 km. Temperature reached the top value as 28.91 °C while RH appeared an increasing order from stage 1 to stage 4. High temperature and RH revealed that WPSH governed Xiamen city. WS were lower in stage 2 and stage 3 when the WPSH fluctuated than that in stage 1 and stage 4. South and east wind were the predominated but WD varied from time to time (Fig. S2). In general, WPSH activity directly influenced the surface layer parameters which demonstrated different trend, and the covariations indicated a synoptic-scale impact (Roger and Andrew, 2002).

Vertical distribution of aerosol could reveal the generation, evolution, dissipation and pathway of particulate matter pollution. Fig. 3 depicts vertical distribution (from 100 to 3000 m) of aerosol b_{ext} during this period. The b_{ext} range was from 0 to 500 Mm^{-1}, which could cover extinction coefficient scale in lower layer. It could also recognize surface layer pollution from high altitude status. Extinction contribution came from surface since the period that could possibly artificially classified this episode as a weak transport pollution subsequently pluses cumulative growth (subjectively). Air pollution was dominated by vertical mixing process from bottom to top since late 17th, Sep. Stagnant atmosphere ensued with lower WS in surface layer which accelerated the accumulation of pollutants. Residual layer was an indicator of surface layer particles dissipation. Note that residual layers appeared twice when were from the midday of 19th to 20th and 23rd to the end, as well as the improved air quality. Air pollutants accumulated in 1 km around basically in the lower layer. Time series of vertical extinction distributed synchronously with surface layer pollutants which are displayed in Fig. S3.

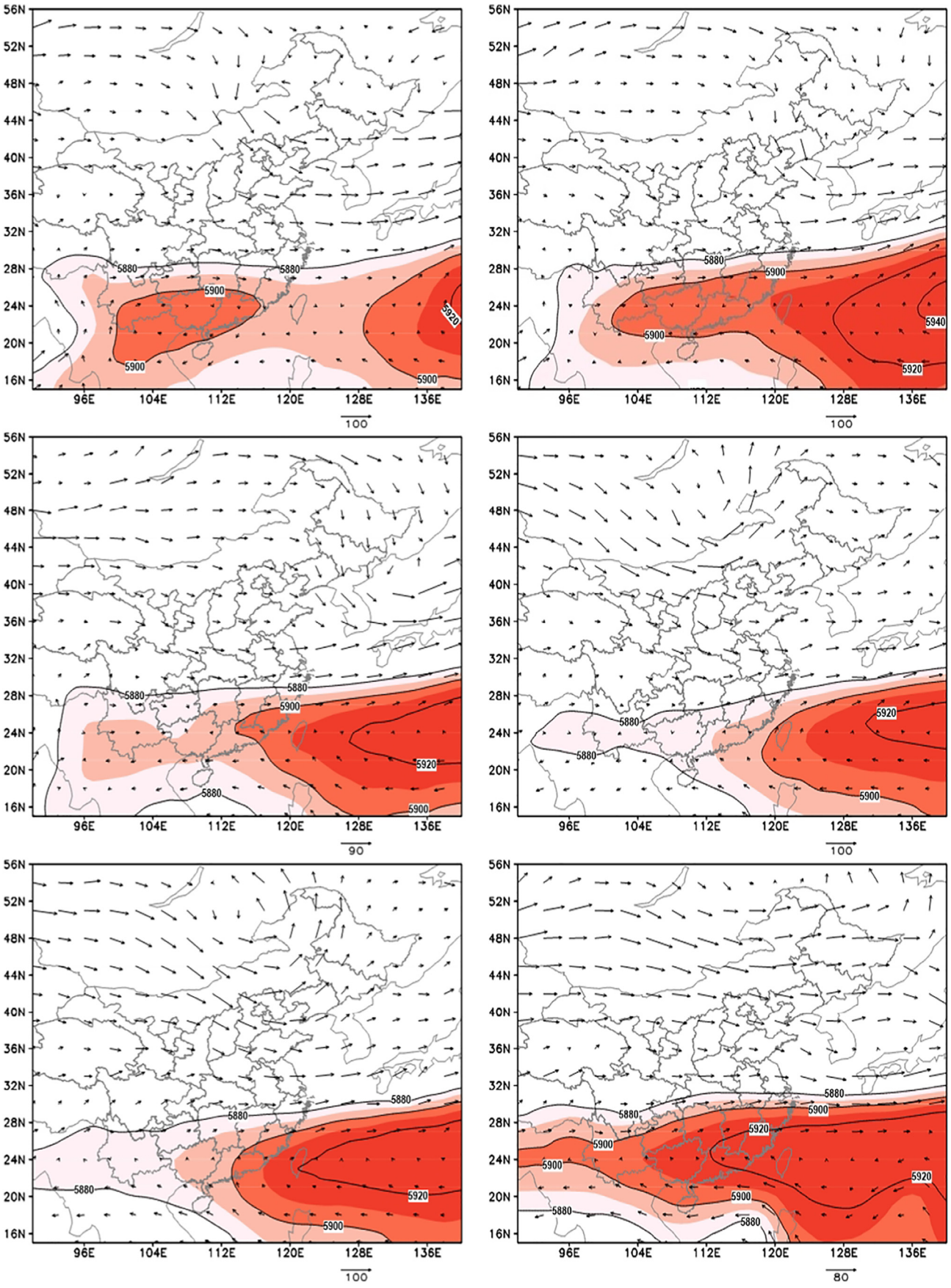

Fig. 1. Synoptic situations at 500hpa from 18th to 23rd Sep. The gradient color area indicates the WPSH over the map and contour line was from the characteristic isoline of 5880 gpm to the center isoline of 5920 gpm.

Table 1
Synoptic situation and meteorological parameters in four stages.

Parameters	Stage 1	Stage 2	Stage 3	Stage 4
WPSH activity	Merged and eastern shifted slowly	Eastern shifted with fluctuation	Western shifted with fluctuation	Western shifted and control
Visibility/km	19.37 ± 4.30	15.57 ± 2.91	10.95 ± 2.22	18.24 ± 4.30
Mixing layer height/km	1.43 ± 0.60	1.13 ± 0.30	0.86 ± 0.14	1.05 ± 0.39
T/°C	28.02 ± 1.22	27.82 ± 1.25	28.88 ± 0.99	28.91 ± 1.11
RH/%	74.41 ± 6.33	75.59 ± 5.71	81.30 ± 5.89	82.63 ± 5.78
WS/m·s^{-1}	1.19 ± 0.44	0.97 ± 0.43	0.96 ± 0.35	1.13 ± 0.42

3.2. Atmospheric oxidation

Atmospheric oxidation reactions will intensify in the proper circumstance with high temperature and intense atmospheric radiation under the control of WPSH. In order to acquire more insights of the impact of oxidation on air pollution episode, atmospheric oxidation O_3, NO_2 and O_x ($O_3 + NO_2$) were illustrated in Fig. 4. High concentrations of O_3, accompanied by an ultra-low level of NO_2 were observed during the episode, especially in the midday.

Note that O_3 maintained high value around 100 μg·m^{-3} in the night of 17th, which was the consequence of the weak transport from the merge of WPSH. Low concentration of O_3 and high level of NO_2 revealed the rather weak photochemical activities, which could result in insufficient production of oxidants (OH and H_2O_2 radicals) for gas-phase oxidation (Hua et al., 2008). In stage 2 and 3, the concentrations of O_3 were extremely low in the nights while the O_x still remained high level. Diurnal O_3 varied more obviously than that of NO_2 and concentrations of O_3 and NO_2 were close at night in stage 2 and 3. In general, O_3 governed atmospheric oxidative reaction in daytime while O_3 along with NO_2 dominated oxidation at night. The regulation reflected the daily fluctuation of WPSH to some extent. WPSH ridge moved westward into continent in daytime and retreated eastward into ocean at night. High temperature in middays impelled the formation of O_x and O_3, which was also clearly depicted in Fig. 4. Maximum temperature in each day was corresponding to the highest concentration of O_x entirely in stage 2 and 3. These results could reveal the high rate of photo-chemical reaction rate which was within 1 h.

3.3. Chemical components and influencing mechanism

3.3.1. Overview of $PM_{2.5}$ and chemical components

Fig. 5 illustrates the variation of $PM_{2.5}$ and the determined chemical components of WSIIs and OM during this episode. Compared to Fig. 4, hourly O_3 and $PM_{2.5}$ concentrations showed similar trends which reached the peak values simultaneously during this episode, especially from 19th to 22nd, Sep. This finding was distinct from many studies suggesting that PM and O_3 were at high levels alternatively (Wang et al., 2019). Concentration of O_3 variation in four stages was beyond expectation which was supposed to reveal the similar trend of $PM_{2.5}$, however, the mean values of O_3 decreased from stage 1 to stage 4. As the major components of $PM_{2.5}$, the trends of WSIIs and OM were similar to $PM_{2.5}$. Sulfate (SO_4^{2-}), Nitrate (NO_3^-) of cations and Ammonium (NH_4^+) of anions (SNA) were the dominated ions in total WSIIs. The ions balance of cations and anions is depicted in Fig. S4. The R^2 equaled to 1.0 indicated that the components were identified. The peak values of SNA were up to 50.82 μg/m^3 at 3 o'clock in 22nd when a suspected underlying local emission occurred. The local event was probably caused by industrial zone southwestwards to the observation sites in the midnight when the wind direction turned southward, which also caused peak values of SO_2 and CO (Fig. S3). Slightly differences of chemical components proportions between four stages were clearly depicted. Organic matters stayed higher proportion of 41.9% in stage 1 than that in stage 2 to stage 4. SNA proportions showed an opposite tendency in four stages against that of OM. Nitrate and ammonium proportions increased slowly while OM increased from stage 1 to 3. Sulfate and EC proportion was different to other components. Sulfate was considered as secondary generation production while EC was primary emission contaminate, which could confirm the sophistication of this episode governed by WPSH. In order to distinct the different contributions to the episode of weekday/weekend sources and WPSH, time series of PM2.5 concentrations of four weeks in September are illustrated in Fig. S5. PM2.5 concentrations in weekday were obviously higher than that of weekend in four weeks. The stages division based on synoptic situation occasionally covered the weekday and weekend: stage 1 and 4

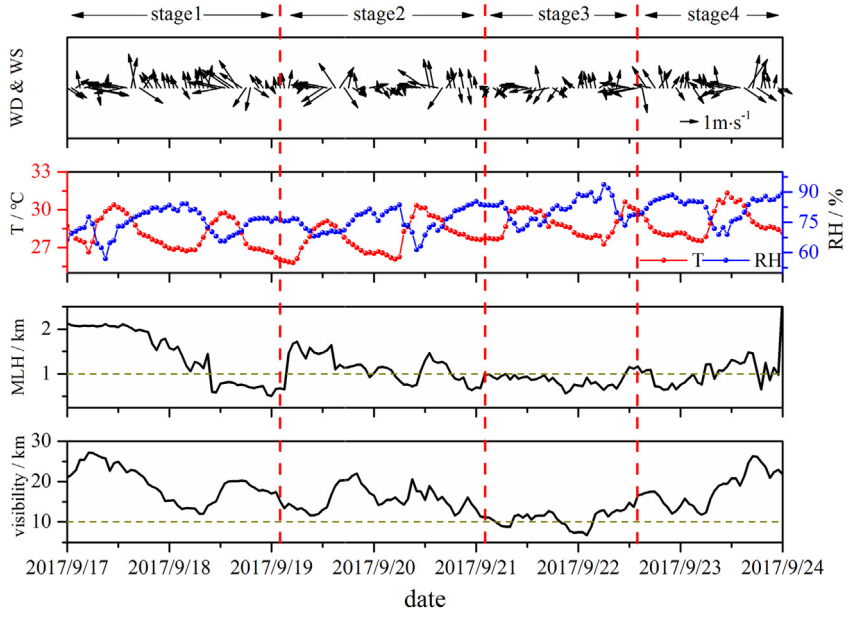

Fig. 2. Time series of WD, WS, temperature, relative humidity, mixing layer height and visibility during the episode.

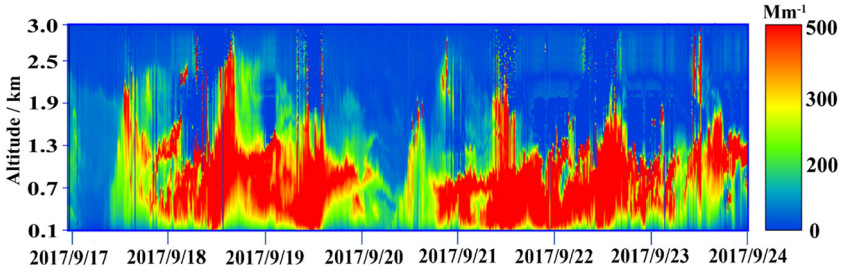

Fig. 3. Pseudo color map of aerosol extinction coefficients during observation periods. Vertical direction stands for variation of coefficients in different altitude. Altitudinal resolution is 7.5 m. Blind area is below 0.1 km so that altitude scale was selected from 0.1 to 3.0 km which covered mixing layer. The color batch ranged from 0 to 500 Mm^{-1}.

had days on the weekend while stage 2 and 3 were in the middle of the week. It appeared that the pollution in stage 2 and 3 was more serious than that in stage 1 and 4. Compared with the other 3 weeks, WPSH really strengthened the air pollution as an amplifier during the episode. The high temperature and oxidation resulted from WPSH accelerated the oxidation rate in atmosphere and finally caused this air pollution.

Box charts of OC, EC and OC/EC ratio are exhibited legibly in Fig. 6. Carbon aerosol contained OC and EC. EC tracer method was used to estimate the SOC content in this paper and the converting factor between OM and OC was chosen as 1.6 (Turpin et al., 2000). EC was emitted from resources directly with incomplete fossil fuel combustion. OC came from two ways: primary organic carbon (POC) and secondary organic carbon (SOC) through photo-chemical reaction. Most of OC and EC existed in fine particulate. The ratio of OC to EC was used to declare the presence and transformation of primary and secondary organic aerosols (Chow et al., 1996; Cachier et al., 1996). OC/EC ratios above 2 indicate the production of SOC. In this paper, OC/EC were all >2 in four stages, which elucidated that secondary generation was the dominated method under the circumstance of high atmospheric oxidation.

NO_3^- and SO_4^{2-} are mainly formed from the transformation of gaseous precursors of NO_2 and SO_2, respectively (Wang et al., 2005). In order to figure the conversions of sulfur to sulfate and nitrogen to nitrate, sulfur oxidation ratios (SOR) and nitrogen oxidation ratio (NOR) were calculated, equations were given in Ohta and Okita (1990). Both SOR and NOR in stage 3 were the highest that indicated high oxidation in the phase of WPSH extended westward. Higher SO_4^{2-} and SOR depended on gaseous SO_2 with active oxidative reactions. The growth of SO_4^{2-} from stage 1 to 3 was clearly captured. Details of SO_4^{2-} and oxidation will be discussed in next section. NO_3^- is a crucial component of $PM_{2.5}$ mass and the percent contribution to the $PM_{2.5}$ mass will vary depending on proximity to NO_2 sources, atmospheric oxidation, gas-phase ammonia concentrations, and environmental variables. As the common precursor of $PM_{2.5}$ and O_3, NO_2 played a key role in atmospheric compound pollution (Pathak et al., 2009), thus NO_2 oxidation was more complicated. NOR were all >0.1 in four stages in the circumstance of high O_x.

3.3.2. Influencing mechanism

The oxidation reactions other than gas-phase oxidation likely explained the formation of abundant secondary sulfate during the episode. The high temperature during the episode was a beneficial factor for aqueous-phase oxidation of SO_2 to sulfate. As an indicator of

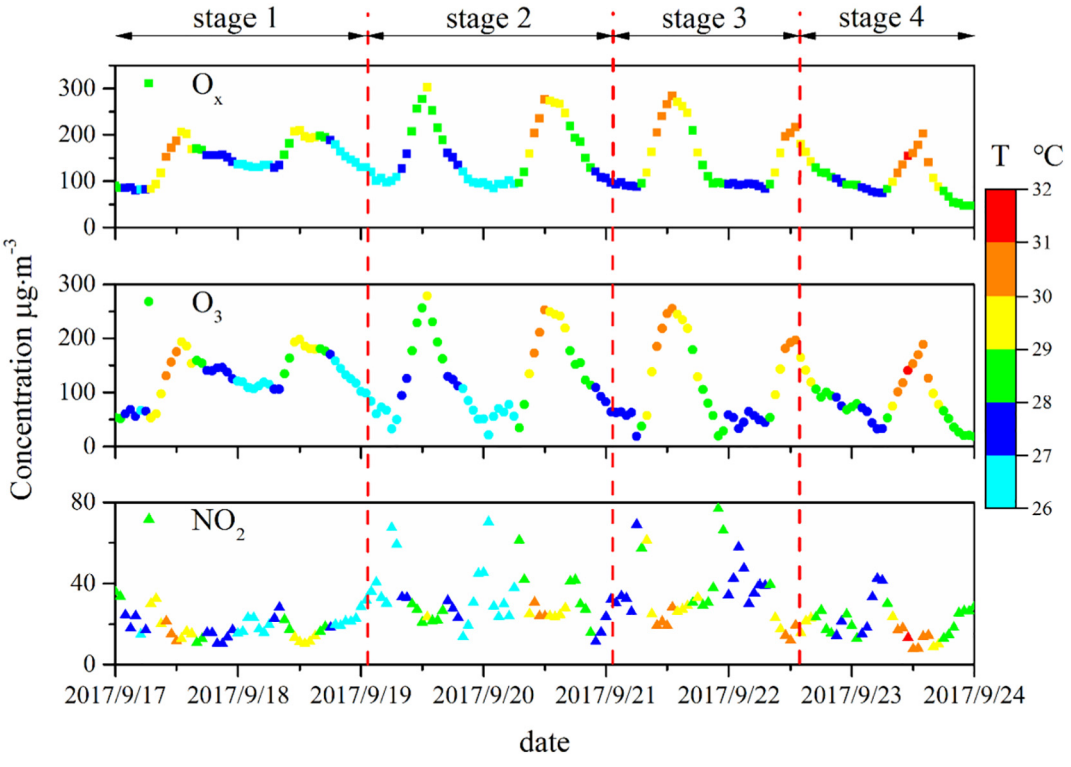

Fig. 4. Variation of O_x (O_3 + NO_2), O_3 and NO_2 during the air pollution episode with the temperature gradient.

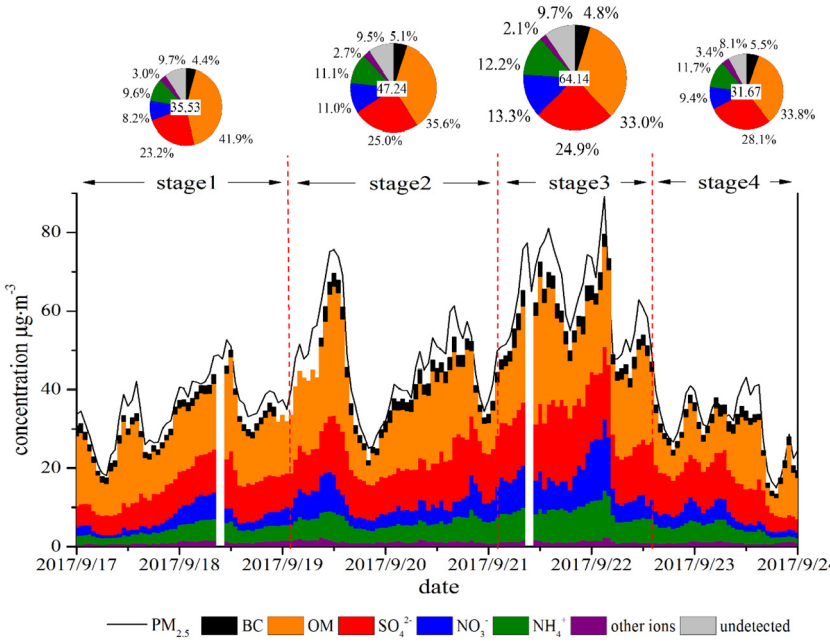

Fig. 5. Time series of $PM_{2.5}$ components and proportions in four stages. $PM_{2.5}$ concentrations in four stages are marked in the center of each pie chart and reflected on pie chart size.

atmospheric oxidation, O_x showed high correlations with some other parameters (Stephens et al., 2008). Practically, SO_2 oxidation proceeded with the following mechanism (Seinfeld and Pandis, 2016):

$$SO_2 + OH + M \rightarrow HOSO_2 + M \quad (4)$$

$$HOSO_2 + O_2 \rightarrow SO_3 + HO_2 \quad (5)$$

$$SO_3 + H_2O + M \rightarrow H_2SO_4 + M \quad (6)$$

where M denoted the molecule in the air. Gaseous H_2SO_4 would further combine with NH_3 to NH_4HSO_4 and/or $(NH_4)_2SO_4$ which were non-volatile. Heterogeneous reactions occurred in consequence that NH_4HSO_4 and $(NH_4)_2SO_4$ formed into particles.

Correlation coefficients between O_x and other parameters were shown in Table S2. Scatter plot of O_x and SO_4^{2-} with temperature gradient in four stages are illustrated in Fig. 7. Positive correlations of four stages were obviously depicted between O_x and SO_4^{2-}. In stage 1 and 4, the slopes were higher than that in stage 2 and 3 when the WPSH fluctuated, which means the generation rates of SO_4^{2-} were faster. However, the gaseous precursor of SO_2 was still at low level. Specifically, O_x concentration was relatively high in stage 1 because of the transportation at the night of 17th. SO_2 concentrations enhanced in stage 2 and 3 so that atmospheric oxidizing reaction occurred with abundant

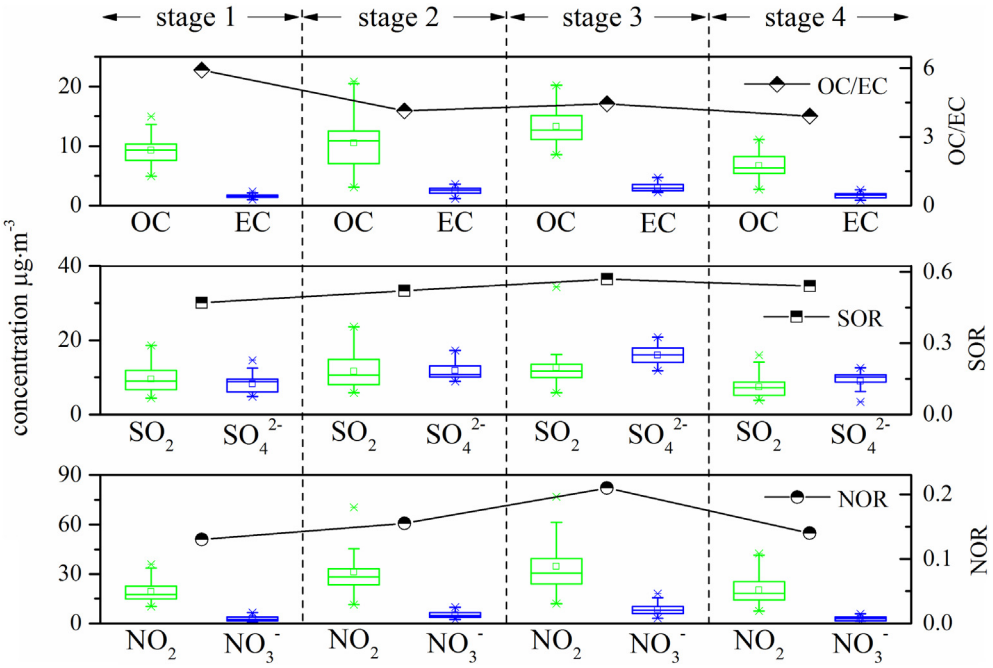

Fig. 6. Box charts of components and ratios in four stages. The range of each box is from 25 to 75 percentile. The long horizontal lines in the boxes are the median values and the small boxes were the average values. The outliers of the parameters are the cross symbols up and under the top and bottom edges. The upper symbols and lines correspond to the variation of OC/EC, SOR and NOR.

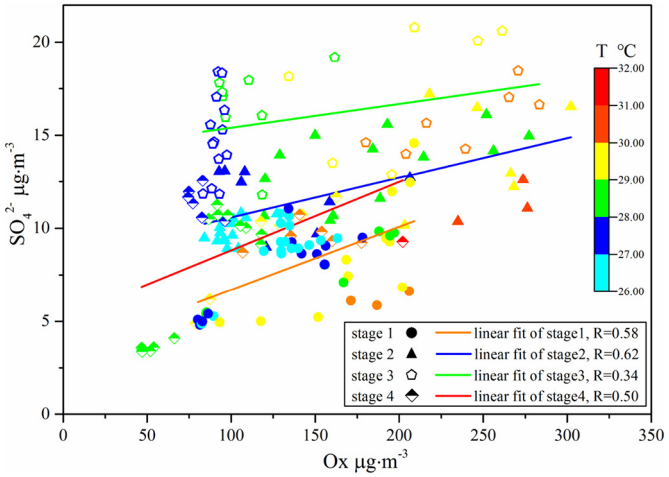

Fig. 7. Scatter plot of O_x and SO_4^{2-} with temperature gradient in four stages.

gaseous precursor. These results revealed the importance of the aqueous-phase reaction for the secondary transformation of SO_2. Local sources like industrial and traffic emissions provided abundant precursors which were also important for secondary pollutants production and resulting air quality deteriorate. Sulfate was primarily in the solid phase indicating that gas-phase oxidation was probably the dominant pathway for sulfate formation. Aqueous phase oxidation likely became predominant at night. Little change between O_x and SO_4^{2-} was collected when the temperature was about 26 °C. Furthermore, a slightly negative growth between O_x and SO_4^{2-} was found when the temperature was at the level of 27 °C. This status altered after the temperature increase beyond 28 °C which was a possible threshold to distinct the atmospheric oxidation capacity. Oxidizing SO_4^{2-} from SO_2 was neglected because of the low reaction rate.

In this paper, significant correlations between NO_3^-/SO_4^{2-} and NH_4^+/SO_4^{2-} while NH_4^+/SO_4^{2-} ratios were all >1.5 (Fig. 8). Nitrate formation is mainly through gas-phase oxidation of NO_2 by oxidation during daylight and the heterogeneous reactions during nighttime (Seinfeld and Pandis, 2016; Kong et al., 2018). As SO_4^{2-} competes with NO_3^- for NH_4^+ during its formation, the relationship between NO_3^- and NH_4^+ at different levels of SO_4^{2-}, which are expressed as NO_3^-/SO_4^{2-} and NH_4^+/SO_4^{2-}, is indicative of the pathway of NO_3^- formation (Pathak et al., 2004, 2009).

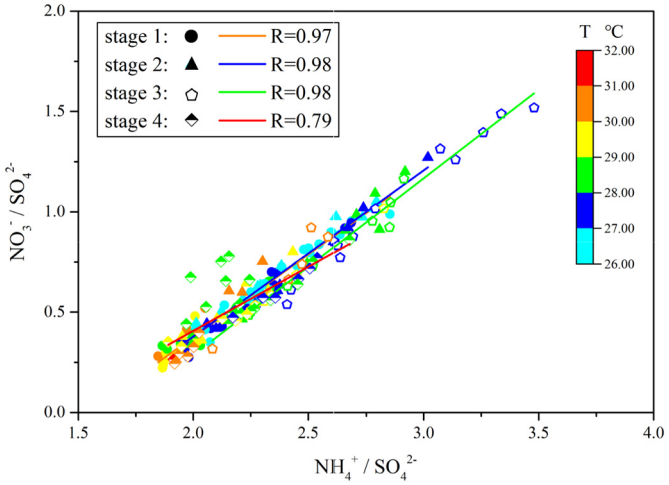

Fig. 8. Molar ratios of NO_3^-/SO_4^{2-} vs. NH_4^+/SO_4^{2-} with temperature gradient in four stages.

Linear correlation between NO_3^-/SO_4^{2-} and NH_4^+/SO_4^{2-} in NH_4^+ rich conditions ($NH_4^+/SO_4^{2-} \geq 1.5$, molar ratio) suggested the homogenous formation of NO_3^-. Compared to Fig. 6, the increase of NOR in stage 2 and 3 under high temperature and high concentration of oxidation may be attributed to heterogeneous reactions for nitrate formation. Ratios of NO_3^-/SO_4^{2-} and NH_4^+/SO_4^{2-} stayed low level when the temperature was >29 °C, which declared increasing rate of sulfate in the circumstance of high Ox. This finding echoed the potential threshold mentioned above and sulfate was probably the key component in $PM_{2.5}$. Sulfate, as a priority of reaction and formation of secondary aerosols, responded to the high oxidation preferentially, followed with nitrate and other compositions of $PM_{2.5}$.

3.4. Optical properties of $PM_{2.5}$

Aerosol extinction influenced visibility directly and was caused by multiple internal factors including pollutant species, concentration, components, size distribution, mixing state and RH (Yan et al., 2015; Deng et al., 2016; Li et al., 2017). Absorption and scattering of aerosol are related to the incident light which caused by different wavelengths. As illustrated in Fig. 9, the trends of $b_{ext,\,rec}$, $b_{ext,\,ret}$, $b_{ext,\,mea}$, and b_{scat} are similar, as well as the $PM_{2.5}$ concentrations. SSA ranged from 0.69 to 0.92 while $b_{ext,\,mea}$ ranged from 55.38 to 464.90 Mm^{-1}. $b_{ext,rec}$ and $b_{ext,\,ret}$ were both calculated by empirical formulas. The formulas contained many aspects and the coefficients of different components were higher in this paper. $b_{ext,\,ret}$ was calculated from Koschmieder equation which reflected the atmospheric visibility. $b_{ext,rec}$ was developed from IMPROVE formula which intended to declare the relative contributions of different chemical components of $PM_{2.5}$. The coefficients of hygroscopic growth, small- and large-size distribution were probably higher because of regional disparity. $b_{ext,\,mea}$ was measured by aethalometer and nephelometer which could represent the local light extinction. The measured light extinction of indraft air was more precise than $b_{ext,rec}$ and $b_{ext,\,ret}$. Correlation coefficients between the optical parameters above in four stages are listed in Tables S3 to S6 and the three kinds of light extinction coefficients were all well fitted. Whereas b_{abs} trend varied little for the reason of minor changes of BC and NO_2 concentrations. Obviously, opposite trend lies between visibility and optical properties.

As the dominated ions of $PM_{2.5}$, SNA were responsible for the air quality deterioration by reason of particles formation and visibility decline due to the contribution of light extinction (Tao et al., 2017). Fig. 10 shows the relationship between measured light scattering coefficients and SNA and OC. Pearson correlation coefficients of the components in four stages were all >0.5 with positive correlations, indicating that secondary inorganic aerosol and OC were the main contributors of aerosol light scattering during this episode. The high correlation coefficients of each stage revealed that the reconstructed light scattering coefficients were adaptive in this site and represented the optical properties of main components of $PM_{2.5}$ basically.

Backward trajectories of four stages during the episode are demonstrated in Fig. 11. Pie charts represent the chemical components contributions in four stages. Air mass mostly came from north in stage 1 and the rest came from east side. The trajectories were well fitted to the WPSH movement of merging. In stage 2, air mass from South Sea probably bring adequate vapor to Xiamen and the trajectories turned to southwest. Stage 3 and 4 trajectories were basically from northeast which WPSH extended westward. Generally, air mass trajectories in four stages were almost accordant to WPSH movement, which could further manifest the stages division of this episode. It is noted that trajectories coupling with aerosol optical properties could declare not only the origination of air mass, but also the effects on local visibility. The results of IMPROVE formula expounded the major contributions to light extinction were ammonium sulfate, ammonium nitrate and OM. Large- and small-represented aged aerosol and new particle formation which was based on Mie theory, respectively (Watson, 2002).

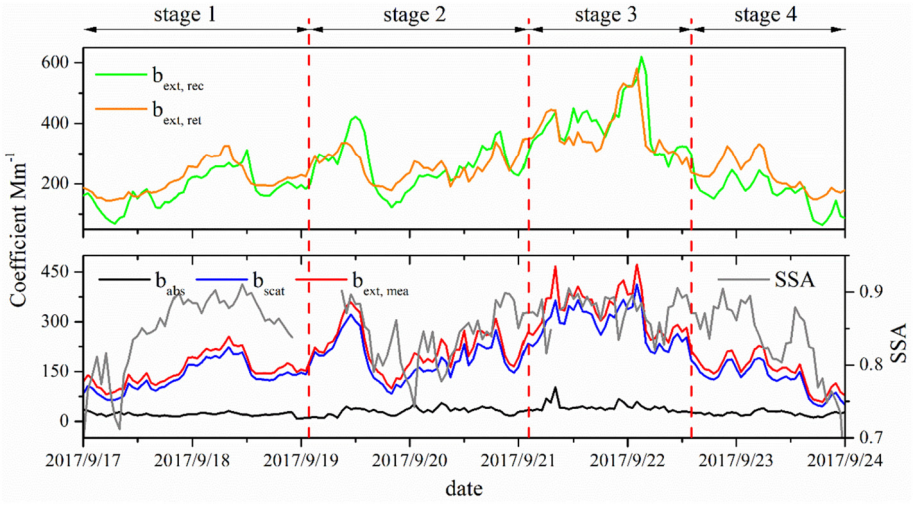

Fig. 9. Temporal variation of $b_{ext,\ rec}$, $b_{ext,\ ret}$, $b_{ext,\ mea}$, b_{scat}, b_{abs} and SSA in four stages.

Large-$(NH)_4SO_4$ and large-NH_4NO_3 contributions increased from stage 1 to 3 then decreased in stage 4 while large-OM contributions decreased from stage 1 to stage 4. Small-$(NH)_4SO_4$, small-NH_4NO_3 and small-OM contributions were on the contrary to that of large-$(NH)_4SO_4$ and large-NH_4NO_3. Apparently, new particle formation rates slowed down in stage 3 and aged inorganic aerosol enhanced step by step, even the relative contribution of aged organic matter was distinct. The continuous influence of high oxidation on aerosol demonstrated obvious internal variation.

4. Conclusions

Formation processes and influencing mechanisms of an air pollution episode were analyzed in Xiamen City in China. Western Pacific

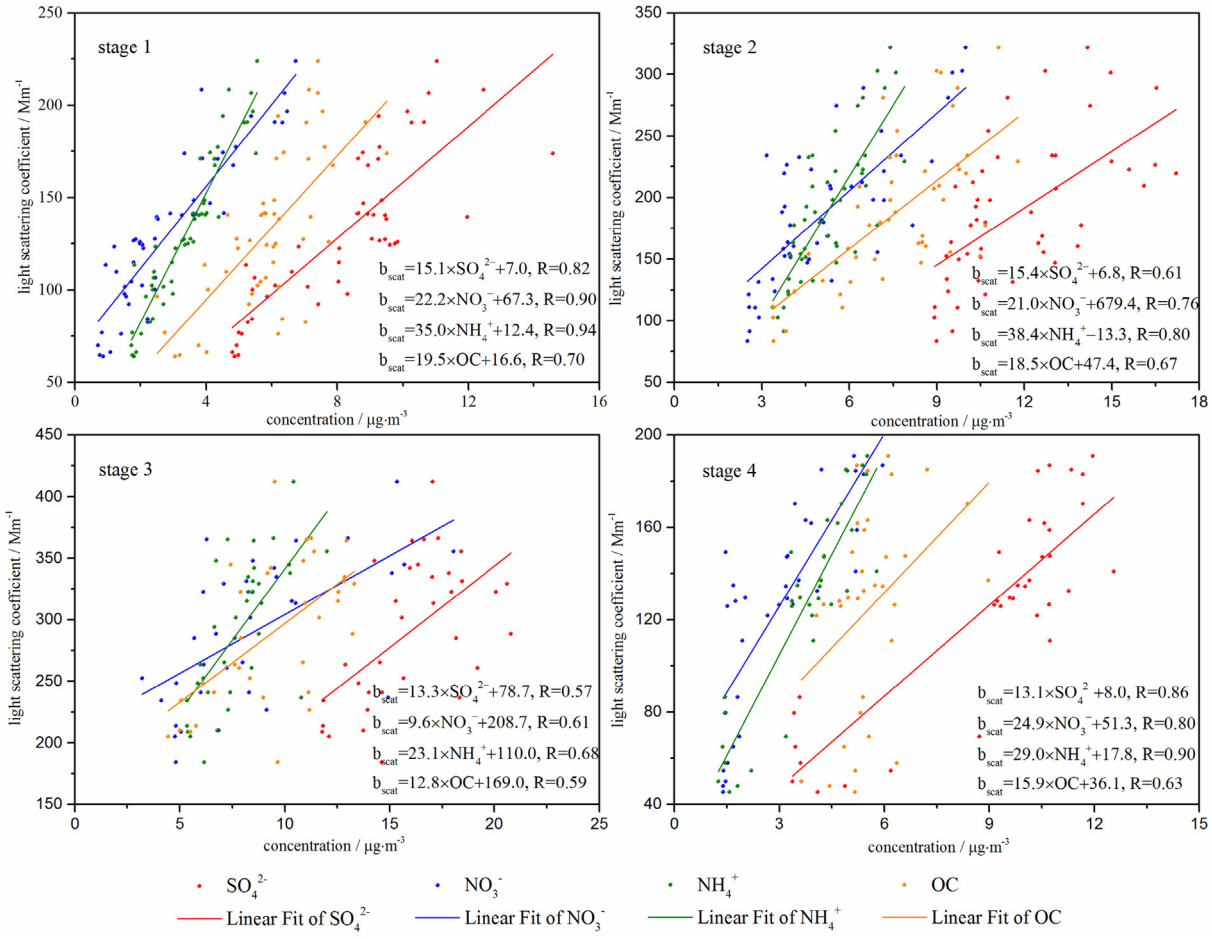

Fig. 10. Correlation between measured light scattering coefficient at 525 nm and sulfate(SO_4^{2-}), nitrate(NO_3^-), ammonium(NH_4^+) and organic carbon(OC) concentration in $PM_{2.5}$ in four stages.

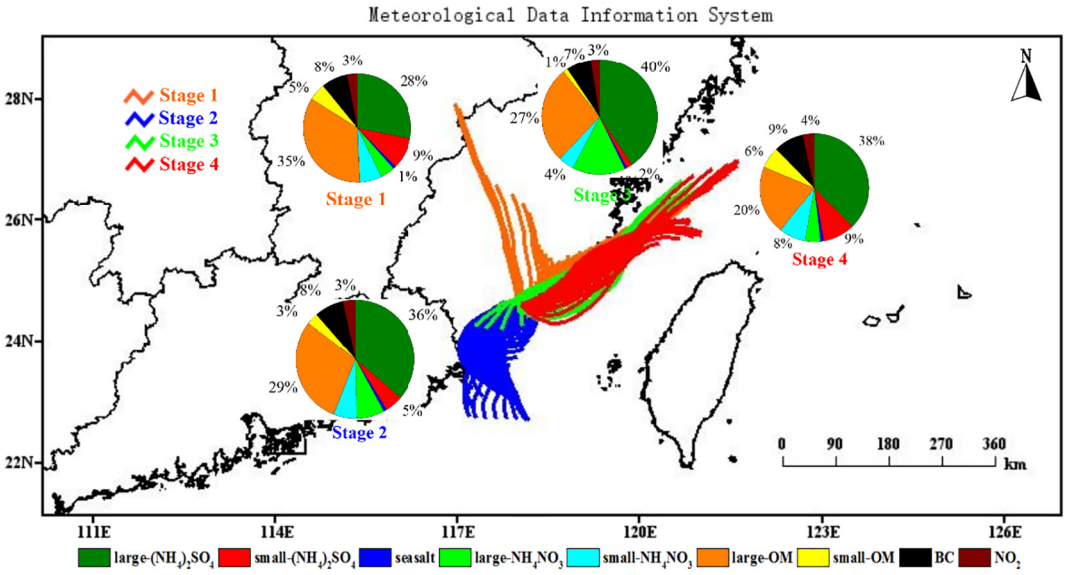

Fig. 11. 24-Hour backward trajectories and pie charts of chemical components contributions in four stages during the episode. The pie charts results were calculated from IMPROVE formula.

subtropical high and consequent high level of oxidation were the dominated factors of this episode. Specifically, this episode in Xiamen was possibly driven by Western Pacific subtropical high with high O_x, temperature and relative humidity. Shifted WPSH at 500hpa, accompanied with slightly variation of wind directions at surface layer, formed a complete situation to derive this episode. WPSH movement caused the ambient air pollution fluctuation, including the atmospheric oxidation, which affected the formation processes and influencing mechanisms. The high level of atmospheric oxidation accelerated the secondary aerosols, which contributed to air pollution with stable meteorology. Secondary aerosol formed through atmospheric photo-chemical reactions, including gas-phase and liquid-phase reactions, in which gaseous precursors were oxidized under the circumstance of high O_x. Chemical components directly/indirectly contributed to aerosol light extinction promotion and the reduction of atmospheric visibility.

Declaration of Competing Interest

The authors declare that they have no conflict of interest.

Acknowledgment

This study was funded by the National Natural Science Foundation of China (41575146), the National Key Research and Development Program (2016YFC02005 & 2016YFE0112200), the Chinese Academy of Sciences Interdisciplinary Innovation Team Project, and Young Talents Projects of Institute of Urban Environment, Chinese Academy of Sciences (Y8L0221B20). The provision of the FNL files from NCEP is appreciated.

Appendix A. Supplementary data

Supplementary data to this article can be found online at https://doi.org/10.1016/j.scitotenv.2019.07.341.

References

Cachier, H., Liousse, C., Pertuisot, M.-H., Gaudichet, A., Echalar, F., Lacaux, J.-P., 1996. African fire particulate emissions and atmospheric influence. In: Levine, J.S. (Ed.), Biomass Burning and Global Change. MIT Press, Cambridge, Mass, pp. 428–440.

Chow, Judith C., Watson, John G., Lu, Zhiqiang, Lowenthal, Douglas H., Frazier, Clifton A., Solomon, Paul A., Thuillier, Richard H., Magliano, Karen, 1996. Descriptive analysis of PM2.5 and PM10 at regionally representative locations during SJVAQS/AUSPEX. Atmos. Environ. 30 (12), 2079–2112.

Davis, R.E., Kalkstein, L.S., 1990. Using a spatial synoptic climatological classification to assess changes in atmospheric pollution concentrations. Phys. Geogr. 11, 320–342.

Deng, J.J., Zhang, Y.R., Hong, Y.W., Xu, L.L., Chen, Y.T., Du, W.J., Chen, J.S., 2016. Optical properties of $PM_{2.5}$ and the impacts of chemical compositions in the coastal city Xiamen in China. Sci. Total Environ. 557-558, 665–675.

Ding, Y.H., 1994. The Summer Monsoon in East Asia: Monsoons Over China. Kluwer Academic, pp. 1–9.

Greene, J.S., Kalkstein, L.S., Ye, H., Smoyer, K., 1999. Relationships between synoptic climatology and atmospheric pollution at 4 US cities. Theor. Appl. Climatol. 62, 163–174.

He, K., Zhao, Q., Ma, Y., Duan, F., Yang, F., Shi, Z., Chen, G., 2012. Spatial and seasonal variability of PM2.5 acidity at two Chinese megacities: insights into the formation of secondary inorganic aerosols. Atmos. Chem. Phys. 12, 1377–1395.

Hua, W., Chen, Z.M., Jie, C.Y., Kondo, Y., Hofzumahaus, A., Takegawa, N., Chang, C.C., Lu, K.D., Miyazaki, Y., Kita, K., Wang, H.L., Zhang, Y.H., Hu, M., 2008. Atmospheric hydrogen peroxide and organic hydro peroxides during PRIDE-PRD'06, China: their concentration, formation mechanism and contribution to secondary aerosols. Atmos. Chem. Phys. 8, 6755–6773.

Kalkstein, L.S., Corrigan, P.R., 1986. A synoptic climatological approach for geographical analysis: assessment of sulfur dioxide concentrations. Ann. Assoc. Am. Geogr. 76, 381–395.

Kong, L.D., Du, C.T., Assiya, Z., Cheng, T.T., Yang, X., Wang, L., Fu, H.B., Chen, J.M., Zhang, S.C., 2018. Trends in heterogeneous aqueous reaction in continuous haze episodes in suburban Shanghai: an in-depth case study. Sci. Total Environ. 634, 1192–1204.

Konor, C.S., Boezio, G.C., Mechoso, C.R., Arakawa, A., 2009. Parameterization of PBL processes in an atmospheric general circulation model: description and preliminary assessment. Mon. Weather Rev. 137, 1061–1082.

Koschmieder, H., 1924. Theorie der horizontalen Sichtweite. Beiträge zur Physik der freien Atmosphäre 12, 33–53.

Li, P.F., Yan, R.C., Yu, S.C., Wang, S., Liu, W.P., Bao, H.M., 2015. Reinstate regional transport of PM2.5 as a major cause of severe haze in Beijing. Proc. Natl. Acad. Sci. U. S. A. 112 (21), E2739–E2740. https://doi.org/10.1073/pnas.1502596112.

Li, R., Hu, Y.J., Li, L., Fu, H.B., Chen, J.M., 2017. Real-time aerosol optical properties, morphology and mixing states under clear, haze and fog episodes in the summer of urban Beijing. Atmos. Chem. Phys. 17, 5079–5093.

Li, Z.Y., Xue, L.K., Yang, X., Zha, Q.Z., Tham, Yee Jun, Yan, C., Louie, Peter K.K., Luk, Connie W.Y., Wang, T., Wang, W.X., 2018. Oxidizing capacity of the rural atmosphere in Hong Kong, Southern China. Sci. Total Environ. 612, 1114–1122.

Lin, J.T., Youn, D., Liang, X.Z., Wuebbles, D.J., 2008. Global model simulation of summertime U.S. ozone diurnal cycle and its sensitivity to PBL mixing, spatial resolution, and emissions. Atmos. Environ. 42, 8470–8483.

Lu, R., 2002. Indices of the summertime Western North Pacific subtropical high. Adv. Atmos. Sci. 19, 1004–1028.

Ohta, S., Okita, T., 1990. A chemical characterization of atmospheric aerosol in Sapporo. Atmos. Environ. 24, 815–822.

Pathak, R.K., Yao, X.H., Chan, C.K., 2004. Sampling artifacts of acidity and ionic species in PM2.5. Environ. Sci. Technol. 38, 254–259.

Pathak, R.K., Wu, W., Wang, T., 2009. Summertime PM2.5 ionic species in four major cities of China: nitrate formation in an ammonia-deficient atmosphere. Atmos. Chem. Phys. 9, 1711–1722.

Petäjä, T., Järvi, L., Kerminen, V.M., Ding, A.J., Sun, J.N., Nie, W., J. Kujansuu, A., Virkkula, Yang, X.Q., Fu, C.B., Zilitinkevich, S. & Kulmala, M., 2016. Enhanced air pollution via aerosol-boundary layer feedback in China, Sci. Rep., 6, 18998, DOI:https://doi.org/10.1038/srep18998.

Pitchford, Marc, Malm, William, Schichtel, Bret, Kumar, Naresh, Lowenthal, Douglas, Hand, Jenny, 2007. Revised algorithm for estimating light extinction from IMPROVE particle speciation data. J. Air Waste Manage. Assoc. 57, 1326–1336. https://doi.org/10.3155/1047-3289.57.11.1326.

Pope, C.A.I.I.I., 2000. Review: epidemiological basis for particulate air pollution health standards. Aerosol Sci. Technol. 32, 4–14.

Ramanatha, V., Crutzen, P.J., Kiehl, J.T., Rosenfeld, D., 2001. Aerosol climate and hydrological cycle. Science 294, 2119–2124.

Roger, G.B., Andrew, M.C., 2002. Synoptic and Dynamic Climatology. Routledge, New York, pp. 735–876.

Seibert, P., Beyrich, F., Gryning, S.E., Joffre, S., Rasmussen, A., Tercier, P., 2000. Review and intercomparison of operational methods for the determination of the mixing height. Atmos. Environ. 34, 1001–1027.

Seinfeld, J.H., Pandis, S.N., 2016. Atmospheric Chemistry and Physics: From Air Pollution to Climate Change. John Wiley & Sons.

Stephens, S., Madronich, S., Wu, F., Olson, J.B., Ramos, R., Retama, A., Muñoz, R., 2008. Weekly patterns of México City's surface concentrations of CO, NOx, PM10 and O3 during 1986–2007. Atmos. Chem. Phys. 8, 5313–5325.

Stevens, B., 2002. Entrainment in stratocumulus topped mixed layers. Quart. J. Roy. Meteor. Soc. 128, 2663–2689.

Sun, Y.L., Du, W., Wang, Q.Q., Zhang, Q., Chen, C., Chen, Y., Chen, Z.Y., Fu, P.Q., Wang, Z.F., Gao, Z.Q., Douglas, R.W., 2015. Real-time characterization of aerosol particle composition above the urban canopy in Beijing: insights into the interactions between the atmospheric boundary layer and aerosol chemistry. Environ. Sci. Technol. 49, 11340–11347. https://doi.org/10.1021/acs.est.5-02373.

Tao, S.Y., Chen, L.X., 1987. A review of recent research on the East Asian summer monsoon in China. Review in Monsoon Meteorology. Oxford Univ. Press, pp. 60–92.

Tao, S.Y., Xu, S.Y, 1962. Circulation characteristics in association with persistent summer drought and flood in the Yangtze-Huaihe River reaches. Acta. Meteor. Sin. 32, 1–10.

Tao, J., Zhang, L.M., Cao, J.J., Zhang, R.J., 2017. A review of current knowledge concerning PM2.5 chemical composition, aerosol optical properties and their relationships across China. Atmos. Chem. Phys. 17, 9485–9518. https://doi.org/10.5194/acp-17-9485-2017.

Trebs, I., Meixner, F.X., Slanina, J., Otjes, R., Jongejan, P., Andreae, M.O., 2004. Real-time measurements of ammonia, acidic trace gases and water-soluble inorganic aerosol species at a rural site in the Amazon Basin. Atmos. Chem. Phys. 4, 967–987.

Turpin, B.J., Saxena, P., Andrews, E., 2000. Measuring and simulating particulate organics in the atmosphere: problems and prospects. Atmos. Environ. 34, 2983–3013.

Wang, Y., Zhuang, G.S., Tang, A.H., Yuan, H., Sun, Y.L., Chen, S., Zheng, A.H., 2005. The ion chemistry and the source of PM2.5 aerosol in Beijing. Atmos. Environ. 39 (21), 3771–3784.

Wang, L., Guan, H., He, J., 2006. The position variation of the West Pacific subtropical high and its possible mechanism. J. Trop. Meteorol. 12, 113–120.

Wang, S.B., Yin, S.S., Zhang, R.Q., Yang, L.M., Zhao, Q.Y., Zhang, L.S., Yan, Q.S., Jiang, N., Tang, X.Y., 2019. Insight into the formation of secondary inorganic aerosol based on high-time-resolution data during haze episodes and snowfall periods in Zhengzhou, China. Sci. Total Environ. 660, 47–56.

Watson, J.G., 2002. Visibility: science and regulation. J. Air Waste Manage. Assoc. 52, 628–713.

Yan, R.C., Yu, S.C., Zhang, Q.Y., Li, P.F., Wang, S., Chen, B.X., Liu, W.P., 2015. A heavy haze episode in Beijing in February of 2014: characteristics, origins and implications. Atmos. Pollut. Res. 6, 867–876.

Zhang, X.Y., Wang, J.Z., Wang, Y.Q., Liu, H.L., Sun, J.Y., Zhang, Y.M., 2015. Changes in chemical components of aerosol particles in different haze regions in China from 2006 to 2013 and contribution of meteorological factors. Atmos. Chem. Phys. 15, 12935–12952.

Zhao, Z.J., Wang, Y.X., 2017. Influence of the West Pacific subtropical high on surface ozone daily variability in summertime over eastern China. Atmos. Environ. 170, 197–204. https://doi.org/10.1016/j.atmosenv.2017.09.024.

Zhuang, B.L., Wang, T.J., Liu, J., Ma, Y., Yin, C.Q., Li, S., Xie, M., Han, Y., Zhu, J.L., Yang, X.Q., Fu, C.B., 2015. Absorption coefficient of urban aerosol in Nanjing, west Yangtze River Delta, China. Atmos. Chem. Phys. 15, 13633–13646.